Sparsity-Based Beamforming to Enhance Two-Dimensional Linear-Array Photoacoustic Tomography

Roya Paridar[a], Moein Mozaffarzadeh[a], Vijitha Periyasamy[b], Manojit Pramanik[b], Mohammad Mehrmohammadi[c], Mahdi Orooji[a,*]

[a] *Department of Biomedical Engineering, Tarbiat Modares University, Tehran, Iran.*
[b] *School of Chemical and Biomedical Engineering, Nanyang Technological University, Singapore.*
[c] *Department of Biomedical Engineering, Wayne State University, Detroit, MI, USA.*

Abstract

In linear-array photoacoustic imaging (PAI), beamforming methods can be used to reconstruct the images. Delay-and-sum (DAS) beamformer is extensively used due to its simple implementation. However, this algorithm results in high level of sidelobes and low resolution. In this paper, it is proposed to form the photoacoustic (PA) images through a regularized inverse problem to address these limitations and improve the image quality. We define a forward/backward problem of the beamforming and solve the inverse problem using a sparse constraint added to the model which forces the sparsity of the output beamformed data. It is shown that the proposed Sparse beamforming (SB) method is robust against noise due to the sparsity nature of the problem. Numerical results show that the SB method improves the signal-to-noise ratio (SNR) for about 98.69 dB, 82.26 dB and 74.73 dB, in average, compared to DAS, delay-multiply-and-sum (DMAS) and double stage-DMAS (DS-DMAS), respectively. Also, quantitative evaluation of the experimental results shows a significant noise reduction using SB algorithm. In particular, the contrast ratio of the wire phantom at the depth of 30 mm is improved about 103.97 dB, 82.16 dB and 65.77 dB compared to DAS, DMAS and DS-DMAS algorithms, respectively, indicating a better performance of the proposed SB in terms of noise reduction.

Keywords: Photoacoustic imaging, beamforming, modelling, sparsity, ℓ_1-norm regularization.

*Corresponding Author: Mahdi Orooji; morooji@modares.ac.ir;

1. Introduction

Photoacoustic imaging (PAI) is a hybrid medical imaging modality that exploits the spatial resolution of ultrasound (US) imaging and the contrast of the pure optical imaging [1, 2, 3]. PAI is based on photoacoustic (PA) effect in which a short laser pulse illuminates the medium. The illuminated pulse is absorbed by the tissue and results in theremoelastic expansion and consequently, wave propagation [4]. The capability of PAI to image the biological tissues has been shown in a wide range of applications such as functional and structural imaging, ocular imaging, tumor detection, imaging the whole body of small animals and blood flow measurement [5, 6, 7, 8, 9, 10]. PAI is divided into two parts: photoacoustic microscopy (PAM) and photoacoustic tomography (PAT), which enables *in vivo* imaging [11]. In PAT, an array sensor in linear, circular or arc shape is used to detect the generated acoustic waves from the surface of the medium [12]. Then, the optical absorption distribution is obtained from the received acoustic waves using a reconstruction algorithm [13]. Algorithms and beamforming methods used in US imaging can be used in PAI with some modifications [14]. One of the most common algorithms used to construct the US and photoacoustic images, is the non-adaptive delay-and-sum (DAS) beamformer, due to its simple implementation and low computational complexity. However, this algorithm results in the reconstructed images with a low resolution and high level of sidelobes. The non-linear delay-multiply-and-sum (DMAS) beamformer is introduced in order to improve the reconstructed images in terms of mainlobe width and sidelobe levels, compared to DAS [15]. Some other beamformers are introduced to enhance the image quality compared to DMAS algorithm, such as Double stage DMAS (DS-DMAS) beamformer which has been developed for linear-array PAI. It has been shown that this algorithm provides a higher contrast compared to DMAS beamformer [16, 17, 18, 19]. Adaptive beamformers are also used to construct the PA images in which the weights are calculated based on the characteristics of the received signals and leads to image improvement in terms of resolution and contrast compared to the non-adaptive beamformers. One of the adaptive beamformers commonly used in Radar applications and US imaging, is Minimum Variance (MV) beamformer [20]. This algorithm rejects the off-axis signals contributions and steers the large sidelobes in the directions where the received energy is low [21]. It has been shown that MV significantly improves the reconstructed images in terms of mainlobe width compared to DAS beamformer. Several modifications have been applied to MV beamformer to enhance the reconstructed images such as temporal averaging, forward-backward (FB) MV, eigenspace-based MV (EIBMV), MV-Based DMAS (MVB-DMAS), sparse MV (SMV) and coherence factor (CF) [22, 23, 24, 25, 26, 27, 28, 29].

Recently, sparse-based methods have been introduced for image reconstruction to enhance the performance of beamformers, in which the problem of the beam-

forming is defined in the way that the difference between the measured signals and the predicted sparse beamformed data (image) is considered to be minimized. Some regularization terms are added to the defined minimization problem in order to improve the image quality and suppress the limited-view artifacts. In [30] a sparse-based method is used in linear-array US imaging in which the forward problem is defined for each row of the image using a set of steering vectors, and the inverse problem is solved in each depth separately. In [31, 32], some regularization terms are introduced and combined with the sparse forward problem to enhance the US images. In [33, 34], the Discrete Fourier Transform (DFT) is used as the sparsifying basis for sparsity to investigate the effect of the regularization term in the frequency domain. In [35], it is shown that the best results would be achieved using the ℓ_1-norm regularization term related to the Laplacian distributed nature of the images.

In this paper, it is proposed to use the sparse-based model in linear-array PAI. The DAS beamformer is defined as a forward problem and the reconstruction is performed using the least squares. Furthermore, a ℓ_1-regularization term is added to the problem following the similar idea presented in [32, 35] in order to improve the reconstructed images and suppress the sidelobes more efficiently. The proposed method, named sparse beamforming (SB), is compared with DAS, DMAS and DS-DMAS beamformers. The results show that a better contrast would be achieved by adding a sparse regularization term to the existing minimization problem, and the noise would be reduced more efficiently compared to other beamformers. Also, the optimum image is obtained using a simple iterative algorithm used in [36].

The rest of the paper is organized as follows. In section 2, a brief explanation about the mentioned beamformers are presented. The proposed method is illustrated in section 3. The results of the numerical and experimental studies are evaluated in section 4 and 5, respectively. Finally, the discussion and the conclusion are reported in section 6 and section 7, respectively.

2. Background

2.1. Beamforming Algorithms

2.1.1. Delay-and-Sum Beamformer

Consider a linear-array transducer consisting of N elements. The output of the DAS beamformer ($y_{DAS}(t)$) is obtained from the following equation:

$$y_{DAS}(t) = \sum_{i=1}^{N} v_i(t - \Delta_i), \tag{1}$$

where t is time index, v_i is the signal received by i^{th} sensor, and Δ represents the time delay. In (1), it can be seen that the received signals are delayed proportional

to the distance between the array elements and the absorber. Then, the delayed signals are summed to construct the optical absorption distribution map of the tissue.

2.1.2. Delay-Multiply-and-Sum Beamformer

DAS is commonly used due to its simple implementation and low computational complexity, as mentioned before. However, the quality of the reconstructed images obtained from this algorithm is not satisfying, since it is not able to reject the off-axis signal contribution and suppress the interference well enough. DMAS, as a non-linear beamformer, is proposed to overcome these limitations and improve the reconstructed images in terms of mainlobe width and sidelobe levels compared to DAS. In DMAS beamformer, the delayed signals are combinatorially multiplied before the summation. The output of the DMAS beamformer is obtained as below:

$$y_{DMAS}(t) = \sum_{i=1}^{N-1} \sum_{j=i+1}^{N} \hat{v}_{ij}(t), \tag{2}$$

where:

$$\hat{v}_{ij}(t) = sign\left(v_i(t-\Delta_i)v_j(t-\Delta_j)\right).\sqrt{|v_i(t-\Delta_i)v_j(t-\Delta_j)|}. \tag{3}$$

Using (2), the reconstructed images would be improved compared to DAS due to the correlation operation which leads to more sidelobe suppression and noise reduction. Note that (3) is used to address the dimensionality squared problem of (2). more information about this algorithm is reported in [15].

2.1.3. Double Stage Delay-Multiply-and-Sum Beamformer

Considering the expansion of DMAS, we have:

$$\begin{aligned} y_{DMAS}(t) = & \underbrace{\left[\hat{v}_{12} + \hat{v}_{13} + \cdots + \hat{v}_{1N}\right]}_{\text{first term}} \\ & + \underbrace{\left[\hat{v}_{23} + \hat{v}_{24} + \cdots + \hat{v}_{2N}\right]}_{\text{second term}} + \cdots \\ & + \underbrace{\left[\hat{v}_{(N-2)(N-1)} + \hat{v}_{(N-1)N}\right]}_{\text{(N-2)\^{}th term}} + \underbrace{\left[\hat{v}_{(N-1)N}\right]}_{\text{(N-1)\^{}th term}}. \end{aligned} \tag{4}$$

It can be seen from (4) that there is a summation procedure inside the DMAS algebra, which is similar to DAS algorithm. DS-DMAS proposes to use DMAS instead of the existing DAS between each term shown in (4). In the other words, another correlation operation is performed between the mutual coupled signals

in DS-DMAS algorithm. The output of the DS-DMAS beamformer is obtained from the following formula:

$$y_{DS-DMAS}(t) = \sum_{i=1}^{N-2} \sum_{j=i+1}^{N-1} \hat{v}_{k_{ij}}(t), \tag{5}$$

where:

$$\hat{v}_{k_{ij}}(t) = sign\left(\hat{v}_{ik}(t)\hat{v}_{jk}(t)\right) . \sqrt{|\hat{v}_{ik}(t)\hat{v}_{jk}(t)|}. \tag{6}$$

$\hat{v}_{ik}$ and $\hat{v}_{jk}$ are the i^{th} and j^{th} term shown in (4), respectively. It has been shown that DS-DMAS improves the reconstructed images in terms of sidelobe levels and resolution compared to DMAS algorithm. More information about this algorithm is reported in [16].

3. Proposed method

In this paper, it is proposed to use the sparse-based model to reconstruct the PA images. The forward problem of the beamforming could be formulated as below:

$$\mathbf{v}_i = \mathbf{A}(i)\mathbf{x} + \mathbf{n}, \tag{7}$$

where $\mathbf{x} \in \mathbb{R}^{N_x N_y}$ is the calculated beamformed data, $\mathbf{v}_i \in \mathbb{R}^M$ is the received signal by i^{th} element, having M time samples, $\mathbf{n}$ is the noise, and $\mathbf{A} \in \mathbb{R}^{M \times N_x N_y}$ is the model matrix. For i^{th} array element, the matrix $\mathbf{A}$ is calculated by the following equation:

$$A_{mn}(i) = \begin{cases} 1 & \text{if } \left|\frac{\mathbf{r}_n - \mathbf{r}_i}{c} - t_m\right| < \Delta t \\ 0 & \text{else} \end{cases}, \tag{8}$$

where $\mathbf{r}_n$ and $\mathbf{r}_i$ are the location vectors corresponding to n^{th} point of the beamforming location and i^{th} element of the transducer, respectively. The t_m is the temporal measurement of m^{th} sample of the received signal, c is assumed to be the speed of sound, and Δt is the temporal interval between each received sample [37]. Note that the matrix $\mathbf{A}$ is data-independent; it is calculated based on the pre-defined geometry of the array sensor and specification of the imaging systems. Referring to the forward problem model defined in (7), the reconstructed image could be obtained from the following Least square (LS) method:

$$\mathbf{x}_{LS} = \underset{\mathbf{x}}{argmin} \left\|\mathbf{A}\mathbf{x} - \mathbf{v}\right\|_2^2, \tag{9}$$

in which the square differences between the received signals ($\mathbf{v}$) and the sparse beamformed data ($\mathbf{A}\mathbf{x}$) should be minimized. It should be noticed that (9) is

an ill-posed problem for $M < N_x N_y$; the system has infinitely solutions. The problem can be solved in a way that we could have a more precise answer by adding the ℓ_p-norm regularization term(s) to the problem. The squared Euclidean norm $\|\mathbf{x}\|_2^2$ is the most familiar regularization term, where the smallest ℓ_2-norm among the solutions is considered to be chosen, called Minimum norm (MN) solution. The squared ℓ_2-norm is a measure of energy [38]. In order to find a more accurate and robust solution, the assumption of sparsity of $\mathbf{x}$ is considered. In this paper, it is proposed to add a ℓ_1-norm regularization term to the existing LS minimization problem. The new minimization problem, named SB, is formulated as follows:

$$\mathbf{x}_{SP} = \underset{\mathbf{x}}{argmin} \, \|\mathbf{A}\mathbf{x} - \mathbf{v}\|_2^2 + \lambda \|\mathbf{x}\|_1 , \tag{10}$$

where SP stands for Sparse. The coefficient λ is a regularization parameter that determines the influence of the added sparse term. The added term could be interpreted as the sparsity of the output (beamformed data) which leads to image improvement and a significant noise reduction. Note that the ℓ_0-norm is the most accurate metric of the sparsity in which the non-zero elements are taken into consideration. However, the ℓ_0-norm results in a non-convex minimization problem. It has been proved that ℓ_1-norm can be an accurate estimation of ℓ_0-norm [39]. Therefore, the regularization term is considered to be ℓ_1-norm in order to make the problem convex. The resulting minimization problem could be solved efficiently using the existing software packages [40, 41]. However, in this work, it is suggested to solve the problem using a simple iterative algorithm [36]. In the following, the problem solving is presented.

3.1. Problem solving

The ℓ_1-norm regularization term added to the minimization problem shown in (10), could be rewritten in the form of $\|\mathbf{x}\|_p^p$ with the consideration of $p = 1$. Therefore, it can be defined as below:

$$\|\mathbf{x}\|_p^p = \sum_{n=1}^{N} |x(n)|^p = \sum_{n=1}^{N} |x(n)|^{p-2} |x(n)|^2 = \|\mathbf{\Phi}\mathbf{x}\|^2, \tag{11}$$

where $\mathbf{\Phi}$ is a diagonal matrix which depends on the beamformed data:

$$\mathbf{\Phi} = \text{diag}\left\{ |x(1)|^{\frac{p-2}{2}}, \cdots, |x(N)|^{\frac{p-2}{2}} \right\}. \tag{12}$$

The motivation behind this scheme is to convert the ℓ_1-norm form into the ℓ_2-norm form, and make the minimization problem solvable. Referring to (10) and (11), the minimization problem would be rewritten as follows:

$$\underset{\mathbf{x}}{argmin} \, \|\mathbf{A}\mathbf{x} - \mathbf{v}\|_2^2 + \lambda \|\mathbf{\Phi}\mathbf{x}\|_2^2 . \tag{13}$$

To obtain the solution, the objective function $L(\mathbf{x})$ is created as below:

$$\begin{aligned} L(\mathbf{x}) &= \|\mathbf{A}\mathbf{x} - \mathbf{v}\|_2^2 + \lambda \|\mathbf{\Phi}\mathbf{x}\|_2^2 \\ &= \mathbf{x}^T\mathbf{A}^T\mathbf{A}\mathbf{x} - 2\mathbf{v}^T\mathbf{A}\mathbf{x} + \mathbf{v}^T\mathbf{v} + \lambda\mathbf{x}^T\mathbf{D}(\mathbf{x})\mathbf{x}, \end{aligned} \tag{14}$$

where $\mathbf{D}(\mathbf{x})$ is a diagonal matrix as below:

$$\begin{aligned} \mathbf{D}(\mathbf{x}) &= \mathbf{\Phi}^T\mathbf{\Phi} \\ &= \text{diag}\left\{|x(1)|^{p-2}, \cdots, |x(N)|^{p-2}\right\}. \end{aligned} \tag{15}$$

Taking the derivation of the objective function with respect to the $\mathbf{x}$, we have:

$$\frac{\partial L}{\partial \mathbf{x}} = 0 \rightarrow 2\mathbf{A}^T\mathbf{A}\mathbf{x} - 2\mathbf{A}^T\mathbf{v} + 2\lambda\mathbf{D}(\mathbf{x})\mathbf{x} = 0. \tag{16}$$

Finally, the beamformed data is achieved from the following iterative algorithm using the all channels together:

$$\mathbf{x}_{SP}^{k+1} = \left(\mathbf{A}^T\mathbf{A} + \lambda\mathbf{D}(\mathbf{x}_{SP}^k)\right)^{-1}.\left(\mathbf{A}^T\mathbf{v}\right), \tag{17}$$

where $(.)^k$ indicates $k^{th}(i = 0, 1, \cdots)$ step of the iteration procedure. Note that this algorithm is not sensitive to the initial beamformed data. In this work, the output of the DAS beamformer is used as the initial beamformed data. The iteration procedure continues until the solution is converged, according to the following criteria:

$$\left\|X_{SP}^{k+1} - X_{SP}^k\right\|^2 \leq \epsilon. \tag{18}$$

The numerical and experimental results in the next section show that the added sparse term leads to a significant image improvement in terms of sidelobe levels and noise reduction, in comparison with other mentioned beamformers.

4. Numerical Results

4.1. Imaging setup

The k-wave MATLAB toolbox is used to simulate the array sensor and the absorbers [42]. An imaging region is designed with the vertical and lateral axis of 40 mm and 20 mm, respectively. An array sensor including 96 elements is used to received the generated PA signals. The central frequency of the array sensor is 5 MHZ with 77% bandwidth. Also, the sampling frequency is 50 MHz. Nine spherical absorbers with the radius of 0.1 mm are positioned along the vertical axis every 5 mm, as initial pressures, beginning from 25 mm of the array sensor.

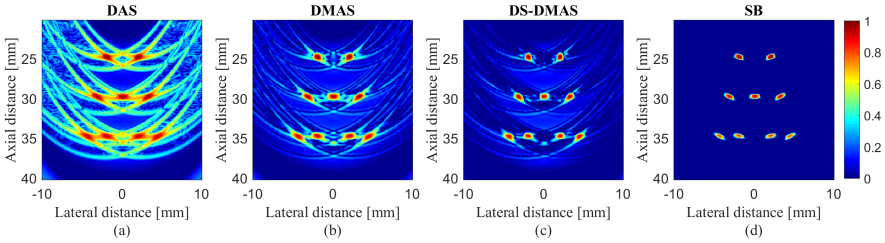

Figure 1: The reconstructed PA images of 9 point targets using (a) DAS, (b) DMAS , (c) DS-DMAS and (d) SB. Noise is added to the received signals having a SNR of 50 dB.

The lateral distance between each two absorbers is 8 mm at the first depth, 6.5 mm at the second depth, 5 mm and 8 mm at the third depth. The speed of sound is assumed to be 1540 m/s. The value of λ is considered to be 0.5. Also, Gaussian noise with the SNR of 50 dB is added to the received signals. Finally, the beamformed signals are Hilbert transformed, normalized and log-compressed to show the reconstructed images.

4.2. Qualitative Evaluation

Figure 1 shows the reconstructed images of the beamformers where 50 dB noise is added to the received PA signals. The reconstructed images using DAS, DMAS, DS-DMAS and SB are presented in Fig. 1(a), Fig. 1(b), Fig. 1(c) and Fig. 1(d), respectively. It can be seen that the reconstructed image obtained from DAS suffers from high sidelobes and low resolution compared to other beamformers. DS-DMAS, as an enhanced version of DMAS, improves the quality of the reconstructed image compared to DMAS, as expected. Comparing DS-DAMS and SB, it can be seen that the proposed SB method leads to significant noise reduction due to the sparse ℓ_1-norm regularization term which is combined with the existing forward model. In the following section, the reconstructed images are evaluated quantitatively to accurately evaluate the performance of the developed algorithm.

4.3. Quantitative Evaluation

In order to evaluate the performance of the beamformers quantitatively, the signal-to-noise ratio (SNR) and full-width-half-maximum ($FWHM$) are utilized. SNR is calculated from the following equation:

$$SNR = 20 \log_{10} P_{signal}/P_{noise}, \tag{19}$$

in which P_{signal} and P_{noise} are the difference between the maximum and the minimum intensity of the reconstructed image, and the standard deviation of the reconstructed image, respectively [16]. The calculated SNRs of the reconstructed images shown in Figure 1 are presented in TABLE 1. It can be seen

Table 1: The calculated SNR (dB) of the images shown in Fig. 1 at different depths.

Depth (mm) \ Beamformer	DAS	DMAS	DS-DMAS	SB
25	42.07	60.72	66.49	157.51
30	39.36	53.17	60.67	141.77
35	32.64	49.45	58.78	110.86

Table 2: The calculated $FWHM$ (mm) of the images shown in Fig. 1 at different depths.

Depth (mm) \ Beamformer	DAS	DMAS	DS-DMAS	SB
25	0.72	0.53	0.38	0.47
30	0.97	0.70	0.50	0.58
35	1.07	0.74	0.53	0.61

that the lowest value of SNR belongs to the non-adaptive DAS beamformer, as expected. DS-DMAS improves the SNR compared to DMAS beamformer. Comparing DS-DMAS and SB, it can be seen that the proposed SB method significantly improves the SNR and leads to better sidelobe suppression, as shown in Figure 1. $FWHM$ is another metrics to evaluate the performance of the beamformers. This metric is used to estimate the spatial resolution and appearance of the reconstructed images. The calculated $FWHM$s are presented in TABLE 2. From the calculated $FWHM$s, it can be seen that DAS results in the highest $FWHM$, and consequently, the lowest resolution in comparison with other beamformers. The proposed SB method improves the $FWHM$ compared to DMAS beamformer. The calculated $FWHM$ obtained from DS-DMAS improves more efficiently compared to SB. However, the differences between the $FWHM$s obtained from these two algorithms are not significant. In fact, the main goal of the proposed algorithm is contrast improvement.

4.4. Imaging at the Presence of High level of Noise

To evaluate and compare the performance of the beamformers at the presence of high level of noise, Gaussian noise is added to the received signals having a SNR of -10 dB. The reconstructed PA images using DAS, DMAS, DS-DMAS and SB are shown in Fig. 2(a), Fig. 2(b), Fig. 2(c) and Fig. 2(d), respectively. It is obvious that the reconstructed image by DAS is more affected by the noise. DMAS improves the reconstructed image and results in higher noise suppression, in comparison with DAS. DS-DMAS improves the image quality compared to DMAS, as expected. Also, it is clear that the proposed SB results in a significant noise reduction, in comparison with other beamformers, and the point targets

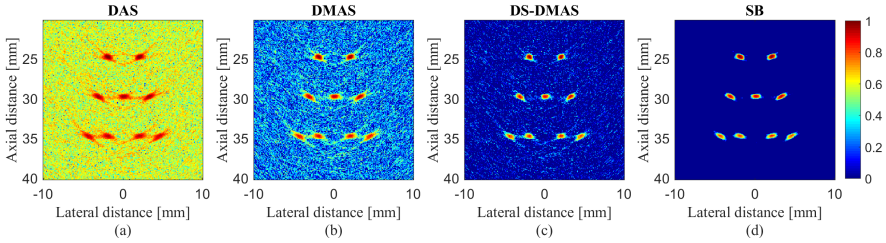

Figure 2: The reconstructed PA images of 9 point targets using (a) DAS, (b) DMAS, (c) DS-DMAS and (d) SB. Noise is added to the received signals having a SNR of -10 dB.

can be clearly seen in all the depths of positioning points. The lateral variations of the reconstructed images shown in Fig.2 are depicted and presented in Fig.3. As it can be seen from the lateral variations, the lowest sidelobes would be achieved using the proposed SB method. Moreover, quantitative results show that the proposed SB method improves the SNR about 66.28 dB, 54.61 dB and 43.19 dB, in average, compared to DAS, DMAS and DS-DMAS, respectively, as presented in TABLE 3. Also, the $FWHM$ value is improved about 0.37 mm and 0.11 mm in average compared to DAS and DMAS, respectively. The calculated $FWHM$ of the DS-DMAS and the proposed SB method is 0.40 mm and 0.47 mm, in average, respectively. It can be concluded that the SB method does not improve the resolution compared to DS-DMAS, as mentioned before. However, the difference between the calculated $FWHM$s is 0.07 mm, indicating that the calculated $FWHM$s, and consequently, the resolutions obtained from DS-DMAS and SB methods are almost close (Fig. 2).

5. Experimental Results

5.1. Wire Phantom

To evaluate the performance of the proposed SB method, the results of the phantom experiments are presented. A Nd:YAG laser pulse with 30 Hz pulse repetition rate at wavelengths of 532 nm is used. To acquire the PA propagated waves, a programmable digital ultrasound scanner (Verasonics Vantage 128) is

Table 3: The calculated SNR (dB) of the images shown in Fig. 2 at different depths.

Depth (mm) \ Beamformer	DAS	DMAS	DS-DMAS	SB
25	30.17	43.19	55.82	103.34
30	28.04	39.43	50.51	91.31
35	26.83	37.41	47.96	89.22

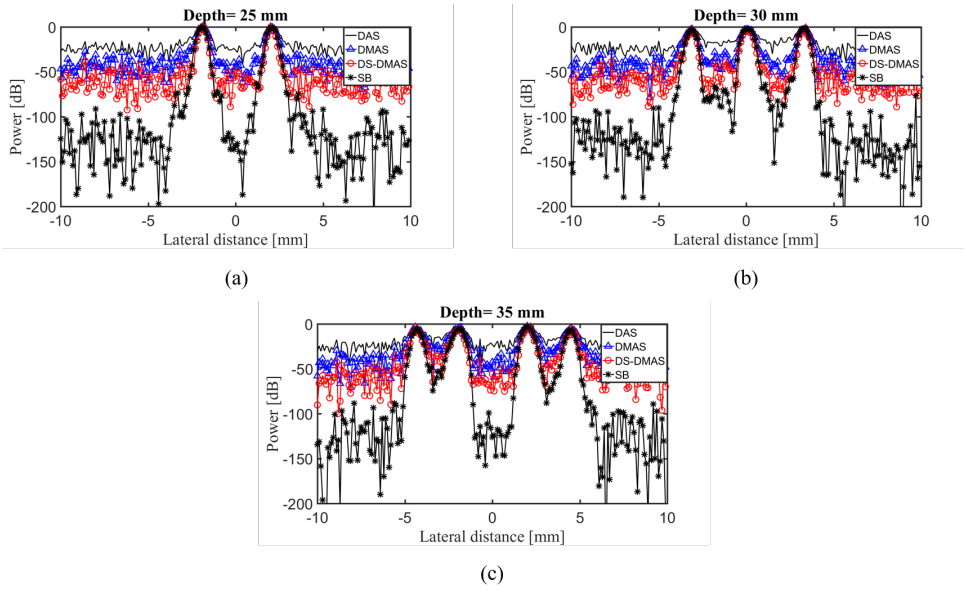

Figure 3: The lateral variations of the images shown in Figure 2 at the depth of (a) 25 mm, (b) 30 mm and (c) 35 mm.

equipped with a linear array transducer (L11-4v), which operates at the frequency range between 4-9 MHz. In order to synchronize the light excitation and acoustic signal acquisition, a FPGA with a high speed is employed. The schematic of the experimental setup is presented in Fig. 4. As it can be seen from the schematic, the laser pulse illuminates the tissue in order to excite the tissue and generate the acoustic waves. Then, the propagated waves are acquired using the linear array transducer. The Verasonics data acquisition and processing platform, which is connected to the linear array, processes the acquired data. Finally, the beamforming algorithm is performed on the stored data to construct the image. Note that

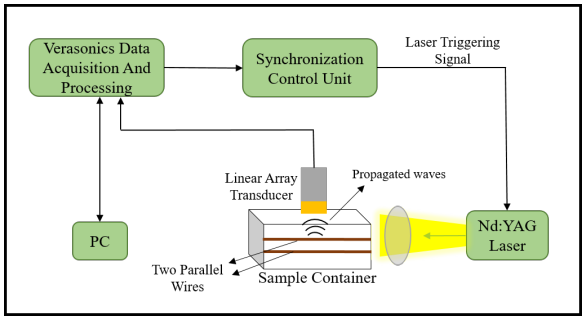

Figure 4: The schematic of the experimental setup.

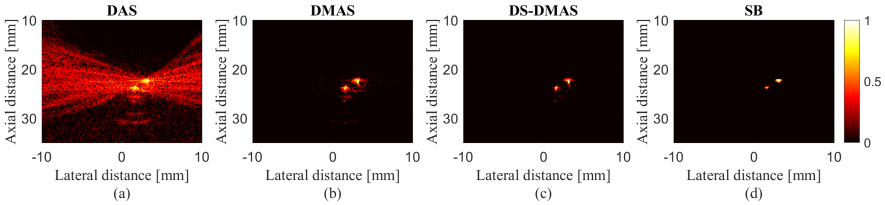

Figure 5: The reconstructed PA images of the wire phantom using (a) DAS, (b) DMAS, (c) DS-DMAS and (d) SB. ($\lambda = 0.5$)

the synchronization control unit, creates a synchrony between the illumination unit and the data acquisition platform, as mentioned before. The wire phantom consists of 2 wires is designed. The wires are positioned 1 *mm* apart form each other in a water tank. It should be noticed that the surface of the linear array sensor is perpendicular to the wire phantom, as shown in Fig. 4. Therefore, it is expected to see the reconstructed wires like two points. In the following, the reconstructed images of the wire phantom obtained from different algorithms are presented.

5.1.1. Qualitative and Qualitative Evaluation

The reconstructed images of the wire phantom are presented in Fig. 5 using the mentioned beamformers. It can be seen that DMAS improved the image quality in terms of resolution and contrast, compared to DAS, as expected. Also, more sidelobe suppression and resolution improvement occurred using DS-DMAS in comparison with DMAS. Comparing the SB method and other beamformers, it can be concluded that the proposed SB beamformer suppresses the sidelobes more efficiently, and it causes the wire targets to be more clearly seen. To evaluate the performance of the beamformers in detail, the lateral variations are presented in Fig. 6 at the depth of 24 *mm*. It is obvious from the lateral variations that SB results in resolution improvement compared to DAS and DMAS algo-

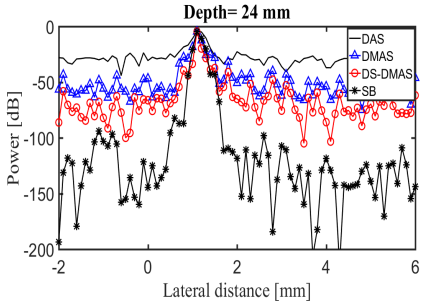

Figure 6: The lateral variations of the reconstructed PA images of the wire phantom shown in Fig. 5 at the depth of 24 *mm*.

Table 4: The calculated CR (dB) for the wire phantom.

Beamformer \ Depth (mm)	22	24
DAS	29.09	5.96
DMAS	51.32	19.47
DS-DMAS	67.29	25.88
SB	133.06	27.48

rithms. Also, the mainlobe width (resolution) obtained from SB is comparable with DS-DMAS beamformer. Furthermore, the level of sidelobes are significantly improved using the proposed SB method compared to other beamformers. The calculated SNRs at this depth show that the proposed method leads to contrast improvement about 71.99 dB, 51.73 dB and 37.68 dB compared to DAS, DMAS and DS-DMAS, respectively. Since the diameter of the reconstructed wire targets are big (like cysts), the contrast ratio (CR) metric can be used to evaluate the performance of the beamformers. CR is defined as the ratio of the mean intensity of the background to the mean intensity inside the target [43]. Higher value of CF indicates a better contrast. TABLE 4 listed the calculated CR for each beamformer. It can be seen that the proposed SB method improved the CR compared to other beamformers.

5.2. Ex vivo Imaging

An *ex vivo* experimental tissue is designed in which two pencils with a diameter of 0.5 mm are embedded inside a chicken breast tissue with dimensions about 4 $cm\times$ 4 cm $\times$ 3 cm. The pencils are 5 mm apart from each other axially. The photograph of the tissue is presented in Fig. 7 (a). Also, each equipment of the imaging system is specified in Fig. 7 (b) and (c). The acoustic waves are detected using a combined linear US/PA imaging probe. Note that the *ex vivo* imaging is performed using the system described in the above section (where the wire

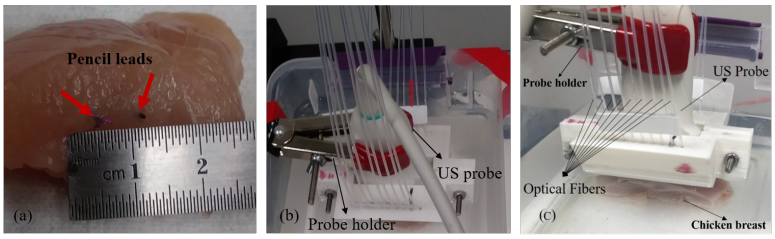

Figure 7: (a) The photograph of the *ex vivo* experimental tissue, (b) the top view and (c) the side view if the imaging setup.

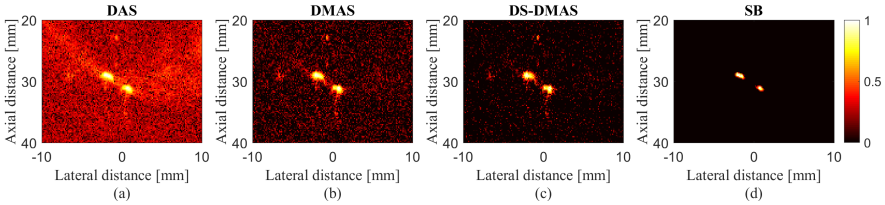

Figure 8: The reconstructed *ex vivo* images using (a) DAS, (b) DMAS, (c) DS-DMAS and (d) SB ($\lambda = 1$).

phantom was used to evaluate the performance of the beamformers). It should be noticed that for the *ex vivo* experiment, the illumination has been conducted from the same side of the probe. As can be seen in Fig. 7, there is a probe holder which carries the US probe along with the optical fibers.

5.2.1. Qualitative and Qualitative Evaluation

The reconstructed images are presented in Fig. 8. As demonstrated, DAS leads to the lowest resolution and contrast. DS-DMAS provides a higher resolution and also leads to more noise reduction compared to DMAS. It is obvious from the figures that the proposed SB method results in significant noise reduction and contrast improvement compared to other beamformers. Note that the background of the *ex vivo* image obtained from SB is darker compared to other beamformers; this indicates the reduced background noise and higher SNR of the proposed method. To conclude the efficient sidelobe suppression caused by SB beamformer more clearly, the lateral variations are shown in Fig. 9 in two different depths. Also, the SNRs of the bemaformers are calculated; the results show that the proposed SB method improves the SNR about 81.48 dB, 72.82 dB and 68.04 dB at the depth of 30 mm, and improves about 87.27 dB, 78.21 dB and 73.76 dB at the depth of 33 mm, compared to DAS, DMAS and DS-DMAS

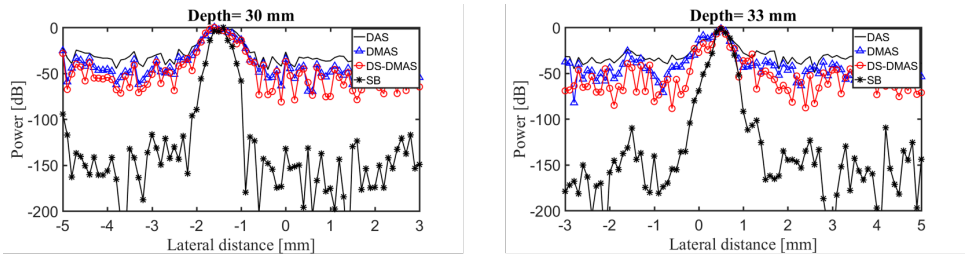

Figure 9: The lateral variations of the reconstructed PA images of the reconstructed images shown in Fig. 8 at the depth of (a) 30 mm and (b) 33 mm.

Table 5: The calculated CR (dB) for *ex vivo* images.

Beamformer \ Depth (mm)	30	33
DAS	28.85	25.71
DMAS	42.17	38.37
DS-DMAS	50.06	46.31
SB	125.24	120.20

algorithms, respectively. Also, the calculated CR shown in TABLE. 5 indicates that the proposed SB method improves the CR for about 95.44 dB, 82.45 dB and 79.03 dB compared to DAS, DMAS and DS-DMAS at in average, respectively.

5.3. In vivo Imaging

The proposed algorithm is also validated for sentinel lymph node (SLN) imaging of rat [44, 45]. The Nd:YAG pump laser (Continuum, Surelite Ex, San Jose, California) operated at 10 Hz is used to illuminate the sample at 1064 nm. A fiber bundle of 1600 multimode fibers are used to guide the laser beam to the animal. The generated PA signals are acquired using a 128 element array clinical ultrasound system (E-CUBE 12R, Alpinion, South Korea). The transducer is 3.85 cm $\times$ 1 cm with a center frequency of 8.5 MHz and a fractional bandwidth of 95% [46, 47]. Adult Sprague Dawley rat of 250 gms is initially anesthetized using ketamine (85 mg/kg) and xylazine (15 mg/kg). Inhalation anesthesia of 1 L/min oxygen and 0.75% isoflurane (Euthanex Corp.) is used to maintain the animal under anesthesia during the experiment. The fur on the region of interest is removed using a hair clipper and hair removal cream (Veet, Reckitt Benckiser). A 5 mm thick chicken breast tissue is placed on the animal to mimic SLN imaging of a human. Black ink is injected in the forepaw of the animal and massaged for the ink to flow into the lymph node. Laser energy of 20 mJ/cm^2, which is within the maximum permissible limit of 100 mJ/cm^2 for 1064 nm as per American National Standard for Safe Use of Lasers is used to illuminate the region of interest. After the acquisition of PA images, the animal is euthanized with an overdose of pentobarbital. All experiments are performed in accordance with the guidelines and regulations approved by the Institutional Animal Care and Use Committee of Nanyang Technological University, Singapore (Animal Protocol Number ARF-SBS/NIE-A0263).

5.3.1. Qualitative and Qualitative Evaluation

The reconstructed images of the SLN experiment are presented in Fig. 10. It can be seen from the figures that the quality of the reconstructed images obtained from DAS is not well enough, having low resolution and high level of noise.

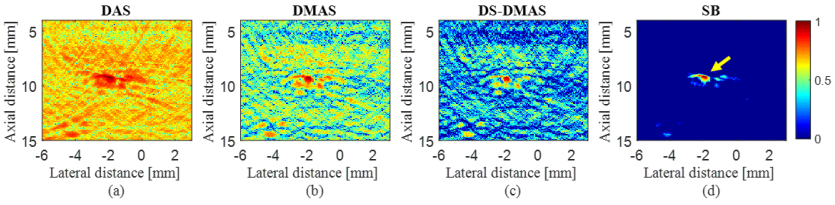

Figure 10: The reconstructed images of the *in vivo* experiment using (a) DAS, (b) DMAS, (c) DS-DMAS and (d) SB ($\lambda = 1$). The yellow arrow in (d) shows the reconstructed SLN.

Comparing DMAS and DS-DMAS, it can be seen that DS-DMAS improves the quality of the reconstructed image and suppresses the sidelobes more efficiently. The proposed SB method significantly suppresses the noise and improves the contrast compared to other mentioned methods; The reconstructed SLN, shown with the yellow arrow in Fig. 10 (d), can be more clearly seen using the SB method compared to other mentioned methods. Also, quantitative results show that SB leads to SNR improvement about 51 dB, 46.41 dB and 40.21 dB compared to DAS, DMAS and DS-DMAS, respectively.

6. Discussion

The main enhancement obtained by the proposed SB method is image improvement in terms of noise reduction in comparison with other beamformers. The reconstructed images obtained from DAS have low resolution and high sidelobes, since this algorithm cannot reject the contribution of the off-axis signals due to its non-adaptive property. DMAS, as a non-linear beamformer, improves the reconstructed images compared to DAS; the combinatorially multiplication in DMAS rejects the off-axis signal contribution and leads to more noise reduction compared to DAS. However, the reconstructed images obtained from DMAS still suffers from high sidelobes. DS-DMAS, as a modify version of DMAS algorithm, improves the image quality in terms of mainlobe width and sidelobe levels compared to DMAS due to the usage of another correlation process instead of the existing DAS algebra inside DMAS algorithm. Sparse-based model algorithms have been developed recently in order to suppress the sidelobes more efficiently. This kind of algorithms have a wide range of applications in computed tomography (CT) and US image formation in which the forward problem of the beamformer is defined. Then, a regularization term is added to the defined model to improve the image quality. Different types of regularization terms exist which are based on the image itself (e.g. total variation) or the local approximation of the image pixels (e.g. wavelets or discrete cosine transform). Each of these regularizers can be a separate topic for study. In this work, the ℓ_1-norm regularization term is chosen to be studied. Combining the ℓ_1-norm regularization

term to the forward problem definition of the beamforming, the sidelobes would be suppressed significantly compared to other mentioned beamformers. In the other words, adding the ℓ_1-norm regularization term means that the beamformed data is considered to be sparse. This assumption leads to more noise reduction and contrast improvement as shown in Fig. 1, Fig. 8 and Fig. 10. A main improvement obtained by the proposed method is higher contrast (lower sidelobes and background noise). As a part of our future studies, we will investigate the potential resolution improvements while the contrast is retained. Note that the images are not sparse themselves; In simulation cases, noise is added to the received signals to make sure that the detected signals are non-sparse. Moreover, the functionality of the proposed SB method is evaluated using the *ex vivo* and *in vivo* experiments where a non-sparse region of interest has been used. As the sparse representations are stable in the presence of noise, it can be concluded that this algorithm is robust against high level of noise, as shown in Fig. 2, due to the sparse term added to the problem. The coefficient λ determines the influence of the sparse regularization term, as mentioned before. In order to evaluate the effect of λ variation on the reconstructed images obtained from the proposed SB method, the reconstruction of the *ex vivo* image is performed using different values of λ. It is obtained that the calculated SNR is increased as the value of λ is increased, as shown in Fig. 11(a). Therefore, the contrasts is improved by increasing λ. Note that the calculated SNR obtained from SB, would be similar to the calculated SNR obtained from DAS for $\lambda = 0$. Also, Fig. 11(b) and Fig. 11(c) show the changes in $FWHM$ and the sidelobe level for different values of λ, respectively. It can be seen that increasing λ results in the reconstructed image with a lower $FWHM$ and sidelobe level, and consequently, a better resolution and more noise reduction. In the other words, by increasing the value of λ, the influence of the sparse regularized term is increased and results in image improvement. Moreover, a simulation is performed in which 14 point targets are positioned along the vertical axis at every 5 mm, starting from 25 mm of the transducers, in order to evaluate the influence of λ in different depths of imaging region. Each two points at each depth are 8 mm away from each other. The reconstructed images obtained from the SB method is presented in Fig. 12 for five different values of λ. It can be seen that as the value of λ increases, more noise reduction occurs at the upper depths, while the deep point targets are disappeared. Therefore, it can be concluded from the results that the parameter λ should be appropriately selected according to different conditions such as depth of imaging, level of noise and etc; too big values of λ may results in disappearance of the deep targets, as shown in Fig. 12, and too small values of λ causes the noise to remain since the influence of the sparse term which leads to noise reduction is decreased [32]. As mentioned before, the minimization problem shown in (10) is solved using a new iterative method. The advantage of solving this minimization prob-

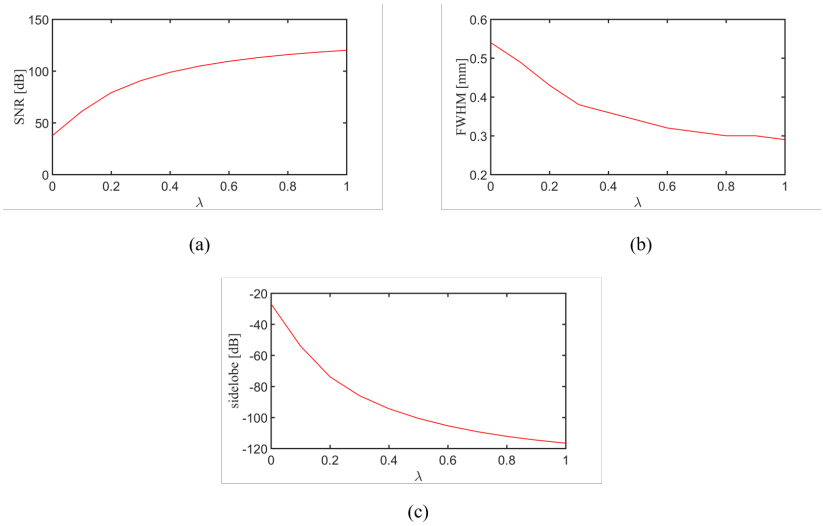

Figure 11: The effect of λ variation on (a) SNR, (b) $FWHM$ and (c) sidelobes.

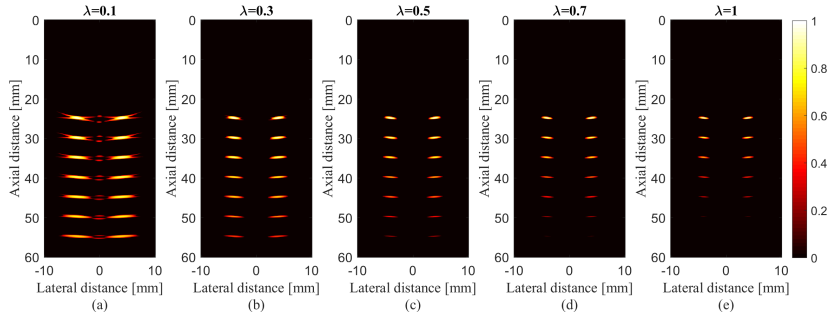

Figure 12: The reconstructed images obtained by the SB method using different values of λ.

lem analytically is that there is no need to use the existing toolboxes. Note that the novelty of the iterative method is that it converts ℓ_1-norm form to ℓ_2-norm form in order to make it possible to used the well-known Least Square method iteratively. Different initial inputs have beet tested in (17) and it has been concluded that there is not difference between the results. It should be noted that the initial input is inversed during the iteration procedure, as shown in (17). It is obvious that the initial input cannot be a vector of zeros since the output would be infinite and the result would be corrupted. Finally, it is worth to mention that the inverse operation in (17) has a high computational burden. In this work, it is proposed to approximate the matrix $\mathbf{A}^T\mathbf{A}$ as a diagonal matrix, since most of the elements of this matrix (except the elements on the diagonal of the matrix) are zero. Also, those non-zero elements have a negligible value compared to the

elements on the diagonal of the matrix. It is known that the inversion of a diagonal matrix is equivalent to the inversion of each element on the diagonal of the matrix, which is not time consuming. It has been concluded that this approximation is almost accurate in this case; The final solution doesn't make a significant difference compared to the case that this approximation is not considered, while the computational complexity is significantly decreased. The processing time of the simulations (Fig. 1) are 0.394 s, 1.131 s, 2.048 s and 5.810 s for DAS, DMAS, DS-DMAS and SB, respectively. Therefore, it can be concluded that DAS has the lowest computational complexity, as expected. The processing time of the DS-DMAS algorithm is higher compared to DMAS. The computation time of SB is higher compared to other mentioned methods. It is worth to note that the computational burden of the proposed SB method is comparable with DS-DMAS while the contrast of the reconstructed image is significantly improved.

7. Conclusion

In this paper, a sparse-based algorithm, named SB method, is performed to reconstruct the PA images. The ℓ_1-norm regularization term is added to the forward problem of the beamforming. Also, the minimization problem is solved using an iterative method. The regularization term added to the forward problem can be interpreted as the sparsity constraint of the output beamformed data which leads to efficiently noise reduction and sidelobe suppression. The simulation results showed that the proposed SB method improves the SNR of the reconstructed image for about 98.69 dB, 82.26 dB and 74.73 dB in average, compared to DAS, DMAS and DS-DMAS, respectively. Also, quantitative evaluation of the experimental results obtained from SB method showed that the SNR is improved about 71.99 dB, 51.73 dB and 37.68 dB for the wire target at the depth of 24 mm compared to DAS, DMAS and DS-DMAS algorithms, respectively. Moreover, the SNR of the *in vivo* image was improved about 51 dB, 46.41 dB and 40.21 dB compared to DAS, DMAS and DS-DMAS, respectively, using the proposed SB method, which indicates the significant improvement in contrast of the reconstructed image. It was shown that the proposed SB method is robust against high level of noise compared to other mentioned beamformers due to the sparse constraint which is forced to the forward problem.

Conflicts of interest

None Declared.

Acknowledgments

This research received no specific grant from any funding agency in the public, commercial, or not-for-profit sectors, and the authors have no potential conflicts of interest to disclose.

References

[1] B. Wang, L. Xiang, M. S. Jiang, J. Yang, Q. Zhang, P. R. Carney, H. Jiang, Photoacoustic tomography system for noninvasive real-time three-dimensional imaging of epilepsy, Biomedical optics express 3 (6) (2012) 1427–1432.

[2] M. Mehrmohammadi, S. Joon Yoon, D. Yeager, S. Y Emelianov, Photoacoustic imaging for cancer detection and staging, Current molecular imaging 2 (1) (2013) 89–105.

[3] P. Beard, Biomedical photoacoustic imaging, Interface focus (2011) rsfs20110028.

[4] M. Xu, L. V. Wang, Photoacoustic imaging in biomedicine, Review of scientific instruments 77 (4) (2006) 041101.

[5] J. Yao, L. V. Wang, Sensitivity of photoacoustic microscopy, Photoacoustics 2 (2) (2014) 87–101.

[6] A. Hariri, J. Wang, Y. Kim, A. Jhunjhunwala, D. L. Chao, J. V. Jokerst, In vivo photoacoustic imaging of chorioretinal oxygen gradients, Journal of biomedical optics 23 (3) (2018) 036005.

[7] S. Y. Nam, S. Y. Emelianov, Array-based real-time ultrasound and photoacoustic ocular imaging, Journal of the Optical Society of Korea 18 (2) (2014) 151–155.

[8] M. Heijblom, W. Steenbergen, S. Manohar, Clinical photoacoustic breast imaging: the twente experience., IEEE pulse 6 (3) (2015) 42–46.

[9] J. Xia, L. V. Wang, Small-animal whole-body photoacoustic tomography: a review, IEEE Transactions on Biomedical Engineering 61 (5) (2014) 1380–1389.

[10] L. Wang, J. Xia, J. Yao, K. I. Maslov, L. V. Wang, Ultrasonically encoded photoacoustic flowgraphy in biological tissue, Physical review letters 111 (20) (2013) 204301.

[11] L. V. Wang, Multiscale photoacoustic microscopy and computed tomography, Nature photonics 3 (9) (2009) 503–509.

[12] M. Nasiriavanaki, J. Xia, H. Wan, A. Q. Bauer, J. P. Culver, L. V. Wang, High-resolution photoacoustic tomography of resting-state functional connectivity in the mouse brain, Proceedings of the National Academy of Sciences 111 (1) (2014) 21–26.

[13] M. Xu, Y. Xu, L. V. Wang, Time-domain reconstruction algorithms and numerical simulations for thermoacoustic tomography in various geometries, IEEE Transactions on biomedical engineering 50 (9) (2003) 1086–1099.

[14] C.-W. Wei, T.-M. Nguyen, J. Xia, B. Arnal, E. Y. Wong, I. M. Pelivanov, M. O'Donnell, Real-time integrated photoacoustic and ultrasound (paus) imaging system to guide interventional procedures: ex vivo study, IEEE transactions on ultrasonics, ferroelectrics, and frequency control 62 (2) (2015) 319–328.

[15] G. Matrone, A. S. Savoia, G. Caliano, G. Magenes, The delay multiply and sum beamforming algorithm in ultrasound b-mode medical imaging, IEEE transactions on medical imaging 34 (4) (2015) 940–949.

[16] M. Mozaffarzadeh, A. Mahloojifar, M. Orooji, S. Adabi, M. Nasiriavanaki, Double-stage delay multiply and sum beamforming algorithm: Application to linear-array photoacoustic imaging, IEEE Transactions on Biomedical Engineering 65 (1) (2018) 31–42.

[17] M. Mozaffarzadeh, A. Hariri, C. Moore, J. V. Jokerst, The double-stage delay-multiply-and-sum image reconstruction method improves imaging quality in a led-based photoacoustic array scanner, Photoacoustics 12 (2018) 22 – 29.

[18] M. Mozaffarzadeh, M. Sadeghi, A. Mahloojifar, M. Orooji, Double-stage delay multiply and sum beamforming algorithm applied to ultrasound medical imaging, Ultrasound in Medicine and Biology 44 (3) (2018) 677 – 686.

[19] M. Mozaffarzadeh, V. Periyasamy, M. Pramanik, B. Makkiabadi, Efficient nonlinear beamformer based on pth root of detected signals for linear-array photoacoustic tomography: application to sentinel lymph node imaging, Journal of Biomedical Optics 23 (12) (2018) 121604.

[20] J. Capon, High-resolution frequency-wavenumber spectrum analysis, Proceedings of the IEEE 57 (8) (1969) 1408–1418.

[21] J.-F. Synnevag, A. Austeng, S. Holm, Benefits of minimum-variance beamforming in medical ultrasound imaging, IEEE transactions on ultrasonics, ferroelectrics, and frequency control 56 (9).

[22] J.-F. Synnevåg, C.-I. Nilsen, S. Holm, P2b-13 speckle statistics in adaptive beamforming, in: Ultrasonics Symposium, 2007. IEEE, IEEE, 2007, pp. 1545–1548.

[23] T. Zhou, Q.-l. Li, X. Chen, T.-f. Wang, S.-p. Chen, Forward-backward minimum variance beamforming combined with coherence weighting applied to ultrasound imaging, in: World Congress on Medical Physics and Biomedical Engineering May 26-31, 2012, Beijing, China, Springer, 2013, pp. 1092–1096.

[24] S. Mehdizadeh, A. Austeng, T. F. Johansen, S. Holm, Eigenspace based minimum variance beamforming applied to ultrasound imaging of acoustically hard tissues, IEEE transactions on medical imaging 31 (10) (2012) 1912–1921.

[25] M. Mozaffarzadeh, A. Mahloojifar, M. Orooji, K. Kratkiewicz, S. Adabi, M. Nasiriavanaki, Linear-array photoacoustic imaging using minimum variance-based delay multiply and sum adaptive beamforming algorithm, Journal of biomedical optics 23 (2) (2018) 026002.

[26] R. Paridar, M. Mozaffarzadeh, M. Mehrmohammadi, M. Orooji, Photoacoustic image formation based on sparse regularization of minimum variance beamformer, Biomed. Opt. Express 9 (6) (2018) 2544–2561.

[27] S.-L. Wang, P.-C. Li, Mvdr-based coherence weighting for high-frame-rate adaptive imaging, IEEE transactions on ultrasonics, ferroelectrics, and frequency control 56 (10).

[28] M. Mozaffarzadeh, Y. Yan, M. Mehrmohammadi, B. Makkiabadi, Enhanced linear-array photoacoustic beamforming using modified coherence factor, Journal of Biomedical Optics 23 (2) (2018) 026005.

[29] R. Paridar, M. Mozaffarzadeh, V. Periyasamy, M. Basij, M. Mehrmodammadi, M. Pramanik, M. Orooji, Validation of delay-multiply-and-standard-deviation weighting factor for improved photoacoustic imaging of sentinel lymph node, Journal of biophotonics (2018) e201800292.

[30] T. Szasz, A. Basarab, D. Kouamé, Beamforming through regularized inverse problems in ultrasound medical imaging, IEEE transactions on ultrasonics, ferroelectrics, and frequency control 63 (12) (2016) 2031–2044.

[31] E. Ozkan, V. Vishnevsky, O. Goksel, Inverse problem of ultrasound beamforming with sparsity constraints and regularization, IEEE transactions on ultrasonics, ferroelectrics, and frequency control.

[32] M. Shen, Q. Zhang, D. Li, J. Yang, B. Li, Adaptive sparse representation beamformer for high-frame-rate ultrasound imaging instrument, IEEE Transactions on Instrumentation and Measurement 61 (5) (2012) 1323–1333.

[33] E. Ozkan, O. Goksel, Inverse problem of ultrasound beamforming with sparsity in time and frequency domain, in: Ultrasonics Symposium (IUS), 2016 IEEE International, IEEE, 2016, pp. 1–3.

[34] T. Chernyakova, Y. Eldar, Fourier-domain beamforming: the path to compressed ultrasound imaging, IEEE transactions on ultrasonics, ferroelectrics, and frequency control 61 (8) (2014) 1252–1267.

[35] T. Szasz, A. Basarab, D. Kouamé, 1-norm regularized beamforming in ultrasound imaging, in: Ultrasonics Symposium (IUS), 2016 IEEE International, IEEE, 2016, pp. 1–3.
[36] X. Jiang, W.-J. Zeng, A. Yasotharan, H.-C. So, T. Kirubarajan, Minimum dispersion beamforming for non-gaussian signals., IEEE Trans. Signal Processing 62 (7) (2014) 1879–1893.
[37] Y. Zhang, Y. Wang, C. Zhang, Efficient discrete cosine transform model–based algorithm for photoacoustic image reconstruction, Journal of biomedical optics 18 (6) (2013) 066008.
[38] A. M. Bruckstein, D. L. Donoho, M. Elad, From sparse solutions of systems of equations to sparse modeling of signals and images, SIAM review 51 (1) (2009) 34–81.
[39] E. J. Candès, J. Romberg, T. Tao, Robust uncertainty principles: Exact signal reconstruction from highly incomplete frequency information, IEEE Transactions on information theory 52 (2) (2006) 489–509.
[40] Y. Zhang, Users guide for yall1: Your algorithms for l1 optimization, Technique report (2009) 09–17.
[41] J. F. Sturm, Using sedumi 1.02, a matlab toolbox for optimization over symmetric cones, Optimization methods and software 11 (1-4) (1999) 625–653.
[42] B. E. Treeby, B. T. Cox, k-wave: Matlab toolbox for the simulation and reconstruction of photoacoustic wave fields, Journal of biomedical optics 15 (2) (2010) 021314–021314.
[43] B. M. Asl, A. Mahloojifar, Eigenspace-based minimum variance beamforming applied to medical ultrasound imaging, IEEE transactions on ultrasonics, ferroelectrics, and frequency control 57 (11).
[44] K. Sivasubramanian, V. Periyasamy, M. Pramanik, Hand-held clinical photoacoustic imaging system for real-time non-invasive small animal imaging.
[45] K. Sivasubramanian, V. Periyasamy, K. K. Wen, M. Pramanik, Optimizing light delivery through fiber bundle in photoacoustic imaging with clinical ultrasound system: Monte carlo simulation and experimental validation, Journal of biomedical optics 22 (4) (2016) 041008.
[46] K. Sivasubramanian, V. Periyasamy, M. Pramanik, Non-invasive sentinel lymph node mapping and needle guidance using clinical handheld photoacoustic imaging system in small animal, Journal of biophotonics 11 (1) (2018) e201700061.
[47] K. Sivasubramanian, V. Periyasamy, R. A. Dienzo, M. Pramanik, Hand-held, clinical dual mode ultrasound-photoacoustic imaging of rat urinary bladder and its applications, Journal of biophotonics 11 (5) (2018) e201700317.